Selective Growth of Graphene-Confined Inkjet-Printed Sn Nanoparticles on Plastic Using Intense Pulsed Light Annealing

Omar Kassem, Vincent Barnier, Mohamed Nasreldin, Jawad Reslan, Asdin Aoufi, Aravindnarain Ravichandran, Sergio Sao Joao, Khalid Hoummada, Ahmed Charai, Mathilde Rieu, et al.

To cite this version:

Omar Kassem, Vincent Barnier, Mohamed Nasreldin, Jawad Reslan, Asdin Aoufi, et al.. Selective Growth of Graphene-Confined Inkjet-Printed Sn Nanoparticles on Plastic Using Intense Pulsed Light Annealing. ACS Applied Materials & Interfaces, In press, 15 (25), pp.30663 à 30673. 10.1021/acsami.3c05015 . emse-04136799

HAL Id: emse-04136799
https://hal-emse.ccsd.cnrs.fr/emse-04136799v1

Submitted on 22 Jun 2023

Selective growth of graphene-confined inkjet-printed Sn nanoparticles on plastic using intense pulsed light annealing

Omar Kassem[1,2], Vincent Barnier[3], Mohamed Nasreldin[1], Jawad Reslan[1], Asdin Aoufi[3], Aravindnarain Ravichandran[1], Sergio Sao-joao[3], Khalid Hoummada[4], Ahmed Charai[4], Mathilde Rieu[2], Jean-Paul Viricelle[2], Thierry Djenizian[1,5], Mohamed Saadaoui[1*]

1. Mines Saint-Etienne, Center of Microelectronics in Provence, Department of Flexible Electronics, F-13541, Gardanne, France

2. Mines Saint-Etienne, Univ Lyon, CNRS, UMR 5307 LGF, Centre SPIN, F - 42023 Saint-Etienne France

3. Mines Saint-Etienne, Univ Lyon, CNRS, UMR 5307 LGF, Centre SMS, F - 42023 Saint-Etienne France

4. IM2NP, Faculté des Sciences de Saint-Jérôme case 142, Aix-Marseille University/CNRS, 13397, Marseille, France

5. Al-Farabi Kazakh National University, Center of Physical-Chemical Methods of Research and Analysis, Tole bi str., 96A. Almaty, Kazakhstan.

Corresponding author: *Email: saadaoui@emse.fr

Abstract

Printing graphene-based nanomaterials on flexible substrates has become a burgeoning platform for next-generation technologies. Combining graphene and nanoparticles to create hybrid nanomaterials has been proven to boost device performance thanks to their complementary physical and chemical properties. However, high growth temperatures and long processing times are often required to produce high-quality graphene-based nanocomposites. For the first time, we report a novel scalable approach for additive manufacturing of Sn patterns on polymer foil and their selective conversion into nanocomposite films, under atmospheric conditions. A combination of inkjet printing and intense flashlight irradiation techniques is studied. Light pulses that are selectively absorbed by the printed Sn patterns cause a temperature of over 1000°C to be reached locally in a split second without damaging the underlying polymer foil. The top surface of the polymer foil at the interface with printed Sn becomes locally graphitized and acts as a carbon source, transforming printed Sn into Sn@graphene (Sn@G) core-shell patterns. Our results revealed a decrease in electrical sheet resistance, with an optimal value ($R_s = 72 \pm 2\ \Omega/\mathrm{sq}$) reached when light pulses with an energy density of 12.8 $\mathrm{J/cm^2}$ were applied. These graphene-protected Sn nanoparticles patterns exhibit excellent resistance against air oxidation for months. Finally, we demonstrate the implementation of Sn@G patterns as electrodes for Li-ion microbattery (LIB) and triboelectric nanogenerator (TENG), showing remarkable performance. This work offers new insight into the development of a versatile, eco-friendly and cost-effective technique for producing well-defined patterns of graphene-based nanomaterials directly on a flexible substrate, using different light-absorbing nanoparticles and carbon sources.

Keywords:

Inkjet printing, Sn nanoparticles, graphene, core-shell nanostructure, intense pulse light, flexible substrate, lithium ion battery, triboelectronic nanogenerator

Introduction

Graphene (G) is a two-dimensional (2D) planar and hexagonal array of carbon atoms with sp^2 hybridization. Since its first isolation by mechanical exfoliation in 2004[1], graphene has been widely regarded as one of the most futuristic materials that would push the frontiers of miniaturization and accelerate the advent of the next-generation ultra-fast electronic devices[2,3]. Owing to its unique nanostructure and outstanding properties, graphene provides promising nanoscale building blocks for the preparation of a variety of graphene-based nanocomposite materials. In particular, graphene-nanoparticles composites (GNPs) have recently gained significant attention, as the coupling of graphene with nanoparticles (NPs) improves the low electrical conductivity of nanoparticles in addition to other physicochemical properties such as work function[4,5] and transparency[6]. GNPs have markedly boosted devices performances in hybrid quantum dots or dye-sensitized solar cells[7,8], transparent conducting films[9], lithium-ion batteries[10,11], catalyst for fuel cells[12], biosensors[13], and many other devices. Furthermore, graphene mechanical properties can be exploited for the development of high elasticity composite materials, a critical requirement for soft and flexible electronics[2,14,15].

Solution processing of electronic devices by printing is an emerging field with many appealing benefits for electronics beyond rigid silicon-based technologies[16–18]. Printing of functional inks on soft substrates like polymer and textile allows shaping of electronics into complex form factors and offers freedom for bending, conforming, and stretching. Moreover, printing provides unique asset of manufacturing in large areas with high throughput. Accordingly, solution-processed GNPs hybrid materials hold promising potential for these next-generation soft electronics such as wearable devices and roll-up displays.

State-of-the-art approaches to synthesis GNPs hybrids include chemical reduction[19], hydro-/solvothermal processes[20], electrochemical deposition[21] and sol-gel[22] . Most of these methods used graphene oxide (GO) since it offers oxygen-terminations that afford chemical anchoring of NPs. Alternatively, GNPs materials have been produced by vacuum-based metallization of reduced graphene sheets using sputtering[23], evaporation[24] and atomic layer deposition[25]. The main drawbacks of these routes include long processing time, the use of vacuum, high annealing temperatures performed in inert or reducing gas, and the use of aggressive chemicals, such as hydrazine, to recover graphene by chemical reduction[26,27]. However, removal of oxygen-groups from the graphene crystal lattice contributes to aggregation, defect formation, and limited solubility[28,29]. The aforementioned factors contribute to scalability and cost issues, which impede the development of solution-processable GNPs on flexible substrates.

To address the current limitations, we have employed intense xenon pulsed light technology (IPL) on metal nanoparticles (MNPs) inkjet-printed on a polymeric foil. Noble metals like Au, Ag are typically the most investigated MNPs in the literature due to their stability and conductivity[30,31], but their high cost and high melting temperatures limit their use in flexible electronics applications. Tin (Sn) is an interesting alternative because it is less expensive and has a lower melting point (232 °C) than noble metals[32]. Furthermore, Sn has long been recognized as an effective catalyst for the formation of graphene multilayers from carbonaceous materials[33]. However, the selection of Sn in GNPs composite production is hampered by two main problems. First, SnNPs oxidize quickly when annealed using a standard thermal process due to their high surface/volume ratio[34,35]. Moreover, Sn decorated graphene prefers to merge into non-percolating aggregates upon annealing at a temperature above the melting point of Sn, as a result of the high surface tension of Sn and its poor wettability on graphene[36,37].

Here, we demonstrate for the first time a versatile, clean and scalable method to form Sn@G core-shell composite material. Uniformly sized SnNPs were synthesized using a modified polyol process, and subsequently dispersed in an appropriate solvent mixture to formulate a stable ink respectful with the printer specifications and compatible with the plastic substrate.

Irradiating such printed SnNPs patterns by intensive xenon light generates extremely localized heating with temperature exceeding 1000°C in a split second, without damaging the polymer foil. The upper surface of the plastic foil locally shrunk and acted as local carbon precursor that diffuses into Sn patterns and form Sn@G composite. As proof of concept, Sn@G materials were successfully integrated as flexible electrodes for lithium-ion microbatteries and triboelectric nanogenerator devices. These demonstrations highlight the scalability and versatility of our strategy for the digital fabrication of future GNPs based devices on flexible substrate. We note that SnNPs and polyimide have been selected for proof-of-concept and believe that many other configurations, including a combination of light-absorbing nanoparticles and solid carbon sources, can be used to produce varieties of GNPs hybrid materials on flexible substrate.

Experimental section

Synthesis of Sn nanoparticles

Sn nanoparticles (SnNPs) were synthesized by polyol method according to the procedure described in the literature[35] with modifications. The synthesis was conducted in a nitrogen-filled glove box at room temperature. 1 g of polyvinyl pyrrolidone polymer (PVP, Acros) with an average molecular weight of 1300 kg/mol and 2 g of sodium borohydride ($NaBH_4$, 99.99%, Sigma Aldrich) were dissolved in 100 ml of diethylene glycol (DEG 99%, Sigma Aldrich). A pre-drying step with molecular sieves (3A 1/16, Acros) was performed for solvents dehydration. The mixture was stirred for 3 hours to obtain a homogeneous and transparent solution. Subsequently, 2 mL of Sn(II) 2-ethylhexanoate ($[CH_3(CH_2)_3CH(C_2H_5)CO_2]_2Sn$, ~ 95%, Sigma-Aldrich) was injected into the solution using a dispenser at the rate of 4.5 mL/min. A black color appears immediately after the injection of Sn precursor indicating the rapid formation of SnNPs. The solution was then stirred for 1 hour. Then, the DEG solvent was repeatedly exchanged by ethanol using centrifugation performed at 6000 rpm for 30 min. The synthesized SnNPs were recovered and dried overnight in vacuum at room temperature.

Sn ink formulation

The synthesized SnNPs were dispersed in Ethanol (EtOH) and ethylene glycol (EG) to obtain an ink with appropriate physical properties for inkjet printing. The Sn ink concentration was 10% wt. The behavior of liquid droplet is dependent on several parameters, essentially the ink viscosity (η), surface tension (γ) and density (ρ) as well as the printhead nozzle diameter (a). These parameters could be combined into the number Z (equation 1), which is defined by the inverse Ohnesorge number and commonly used to predict the printability of a formulation:

$$Z = Oh^{-1} = \frac{\sqrt{\rho.\gamma.a}}{\eta} \qquad (1)$$

It was stated that the Z should be between 1 and 10 for successful inkjet printing[38]. If $Z < 1$, the ink will not jet, whereas the ink is prone to the formation of secondary droplets if $Z > 10$. The viscosity and the surface tension were measured using Brookfield LVDV viscometer and goniometer (Apollo Instrument OCA200), respectively

Inkjet printing

Prior to inkjet printing, the Sn ink was filtered (5µm PTFE filter) to prevent any possible undissolved impurities or NPs agglomeration that may lead nozzle clogging. Then, inkjet printing was done on commercial Dimatix printer (DMP-2800 Fujifilm, Inc., USA). The printer is equipped with 16 nozzles of 21µm diameter with a drop volume of 10 pL (DMC-11610). A 50 µm thick polyimide foil was used as a substrate (Upilex® S-Goodfellow). Prior to printing, the polyimide was cleaned with acetone, isopropanol and water, followed by drying in oven at 100°C for 10 min.

The Sn ink was inkjet-printed using the standard waveform provided by the printer at a voltage of 17 ± 1V and jetting frequency of 5 KHz. The gap between the nozzles plate and the substrate was maintained at 1 mm. The drop spacing was optimized to ensure a good surface coverage when printing a continuous Sn film on Upilex foil. If the drop spacing is too small, bulge instabilities are observed on the edge of printed lines, while no coalescence will occur if the drop spacing value is too important. For our Sn ink, the optimal drop spacing on Upilex foil was set at 25 µm. Finally, the substrate was heated at 40 ºC during printing in order to promote drying of the ink before IPL annealing. The thickness of printed Sn film after drying was around 120 nm.

Intense pulsed light annealing

Inkjet-printed Sn ink was annealed using a Pulse Forge ®3200 X2 tool, (Novacentrix TX, USA). The equipment integrated two xenon stroboscopic lamps delivering radiant energy in a broad light spectrum ranging from 200 to 1500 nm. A train of micro-pulses shaped in different profiles was used to anneal Sn ink. The radiant energy was measured using a bolometer (BX –100, Novacentrix). The samples were kept at a distance of ~3 cm far from the lamps.

Material characterization

Transmission electron microscopy (TEM) was acquired on a Philips CM200 model at 200 kV. The SnNPs were diluted in ethanol, dispensed upon Cu mesh grid and allowed to dry overnight. ImageJ software was used to estimate the SnNPs size distribution and average particle size from TEM images. Microstructural characterization of SnNPs was performed using an X-ray diffractometer (Siemens D5000) with Cu-Kα radiation (λ= 1.54178 Å) at 40 kV and 30 mA over the 2θ range of 25-60°. XRD analyses were done on SnNPs dispersed in ethanol, dropped on (111) silicon wafer and heated at 200 °C. Thermal properties of SnNPs were characterized by simultaneous TGA/DSC with STARe System (Mettler-Toledo) under air. 10 mg of SnNPs were loaded into alumina crucible and experiments were carried out from room temperature to 400 °C under a heating rate of 5 °C/min. Optical absorbance spectra of SnNPs solution and inkjet-printed Sn films were recorded on UV-2600 spectrophotometer (Shimadzu) equipped with an integrating sphere. The surfaces of IPL annealed Sn films were observed using binocular microscope (Nikon SMZ1500). Samples were cross-sectioned using Leica UC6/FC6 ultramicrotome (Leica, Tescan Analytics) at room temperature. The thin films were embedded in an epoxy resin (EpoFix) which cures within a few hours at room temperature. High-Resolution TEM images were performed at 200 keV using a field emission gun Thermo Fisher Titan microscope equipped with a spherical aberration (Cs) correction system. Raman spectra were recorded non-destructively on IPL annealed Sn ink using Horiba Jobin-Yvon / LabRam-HR instrument using an excitation wavelength of 514 nm. The sheet resistance of Sn films was measured using Kelvin structures in a 4-point probing configuration using electric prober (PM5, Suss Microtec).

Electrochemical measurements of Lithium ion battery

The electrochemical characterizations of Sn@G electrodes annealed at 12.8 J/cm² were performed in a Swagelok cell. The half-cells were assembled using a 9 mm disk of Lithium metal working as both counter and reference electrode. A 10 mm disk of whattman glass microfiber was soaked with an organic liquid electrolyte composed of 1M $LiPF_6$ dissolved in a mixture of ethylene carbonate/diethyl carbonate (EC: DEC, 1:1 V/V) and used as a separator. All half cells were assembled in an argon-filled glove box with <0.5 ppm H_2O and <0.5 ppm O_2 atmosphere. The charge/discharge profiles were investigated by chronopotentiometry using the VMP3 potentiostat-galvanostat (Biologic). Cyclic voltammetry (CV) was performed at a sweep rate of 0.05 mV/S within a voltage window of 0 – 3V (*vs*. Li/Li^+). All the specific capacities were calculated according to the total mass of the active material.

Triboelectric Nanogenerator measurements

The output electrical response of the graphene based TENGs was measured using a Keithley 2636 sourcemeter and Stanford low-noise current preamplifier (Model SR570), respectively controlled by LabVIEW program for real-time acquisition. The cyclic compressive force for tribo-electrification was driven by a mechanical linear motor (Linmot, C1100) with a constant displacement of 5 mm and a speed of 0.5 $m.s^{-1}$.

The work function of the test materials was measured using a Non-contactless Kelvin probe system (KP Technology). The measured work functions were compared with the known work function material, (Gold = 4.6 eV). By employing a 100 single point scans on a 1 mm x 1 mm at 72 Hz frequency and 10 V amplitude, the contact potential difference (CPD) is obtained resulting in the work function of the unknown materials.

Results and discussion

SnNPs were synthesized by a modified polyol method. Tin salt was reduced using diethylene glycol and sodium borohydride in the presence of polyvinylpyrrolidone (PVP) stabilizers (see Materials and Methods). The obtained SnNPs are almost spherical with an average size of 10.4 ± 3 nm (Figure 1a). The use of reducing chemicals and long-chain capping agent yields smaller nanoparticles by promoting particle nucleation rate and prohibiting self-aggregation[39]. A high-resolution transmission electron microscopy (HRTEM) image in the inset reveals a core-shell morphology. The fringes in the core correspond to the (200) lattice spacing of a tetragonal β-Sn, in agreement with X-ray diffraction (XRD) (Figure 1b-c). The shell with a thickness of approximately 2 nm comes from the contribution of PVP coating and native tin oxide (SnO_x) layers.

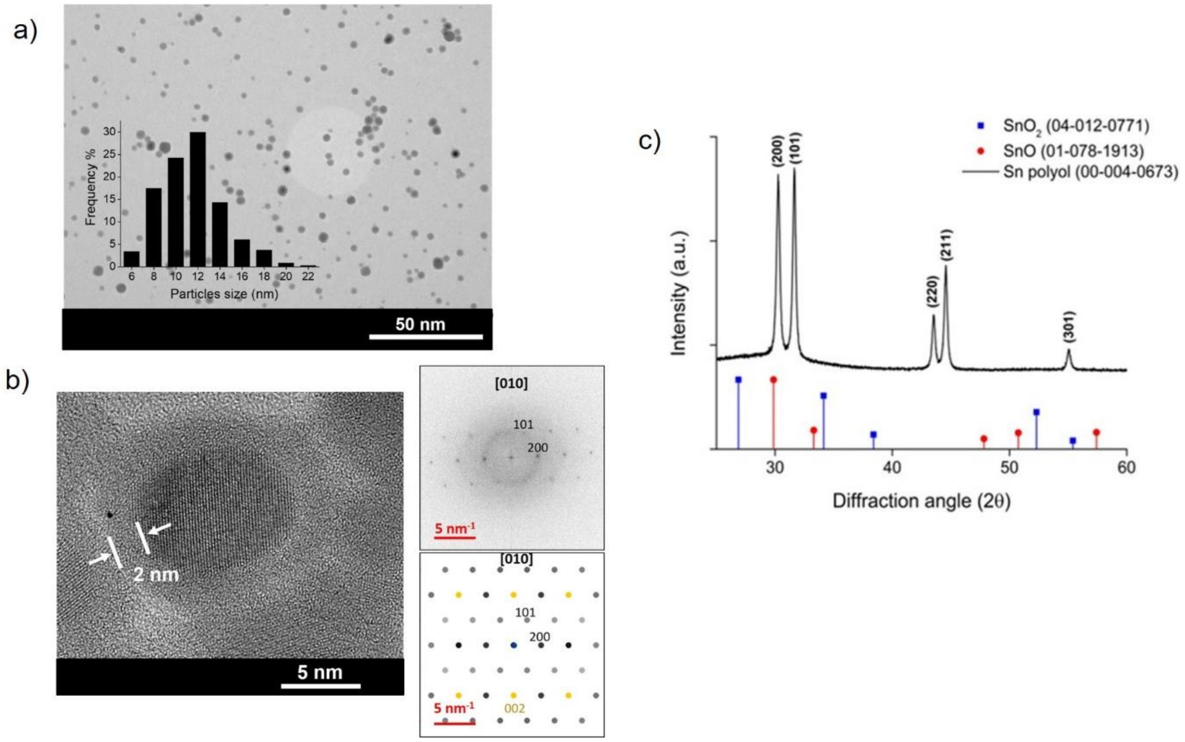

Figure 1 characterization of synthesized SnNPs. (a) TEM image with particle size histograms made by counting 1000 particles (b) HRTEM image of SnNP exhibiting a core-shell structure (c) XRD profile of synthesized SnNPs with corresponding SnO and SnO_2 profiles, according to JCPDS files.

The thermal properties of SnNPs were investigated using TGA/DSC in air, as shown in figure S1. The 4% weight loss observed up to 200°C is attributed to the elimination of adsorbed humidity. The weight increase above 200°C with a sharp exothermic peak (250 °C) in the DSC curve is the signature of the oxidation of metallic SnNPs. A small endothermic peak in the DSC curve is detected at 215 °C, which corresponds to the melting temperature of SnNPs. Compared to the melting temperature of bulk Sn (Tm= 232 °C), these SnNPs exhibit a depression in melting temperature by 17 °C. From the DSC curve, we noticed an endothermic peak at 305-308 °C, corresponding to the decomposition of SnNPs@PVP. For pure PVP, the decomposition temperature is measured at 345 °C, almost 40 °C lower than that for SnNP@PVP. This confirms the role of SnNPs as catalyst for accelerating the decomposition of the PVP.

Following SnNPs synthesis, a 10 wt% Sn ink formulation was engineered with appropriate rheological properties for inkjet printing. Ethanol (EtOH) was chosen due to its ability to disperse and stabilize PVP encapsulated-SnNPs. However, EtOH has low viscosity and surface tension (i.e. η = 1 mPa.s, γ = 22 mN/m) which is unfavorable to form well-defined inkjet droplets with a Z value of ~20, resulting in unsteady printability. To address this problem, we modified the solvents while simultaneously considering solubility, printability and wettability. Ethylene glycol (EG) can be a suitable candidate as an additive due to its high compatibility with ethanol and apposite rheological properties. In addition, it is well known in the literature that the strategy of mixing two solvents with low and high vapor pressure like EtOH (P_{vap} = 5800 Pa) and EG (P_{vap} = 8 Pa) promotes more uniformly printed film by competing for the Marangoni effect and capillary action, and hindering coffee-ring formation upon drying[40,41]. Considering all the aforementioned factors, we found that a 3:7 volume ratio EtOH to EG allows fine-tuning of the viscosity and surface tension to target values of 8 mPas.s and 32 mN/m, respectively. The Z number of the ink is 3.2 predicting reliable printability.

Sn colloid ink, presented in Figure S2a, shows good stability without any visible aggregates for more than a month if it keeps stored in the fridge, and reliable droplet ejection was performed without evident clogging of nozzles (Figure S2b). The surface tension of the ink measured at 32 mN/m is lower than the surface energy of polyimide of 47 mN/m, which ensures nice spherical drop formation on the substrate without the need of any surface treatment (Figure S3).

Inkjet printing of Sn ink resulted in homogeneous patterns. After the drying step at 100°C, the sheet resistance was 1 MΩ/sq. At this step, the SnNPs were still confined into PVP organics that impede the electrons to flow from one NP to the other one. The standard oven annealing with temperature compatible with the use of upilex foil (from 200°C to 350°C, 30 min) resulted in high sheet resistance values ranging from few hundred KΩ up to few MΩ. From the TGA/DSC results, the increase of annealing temperature of printed SnNPs ink will tend to evaporate organic solvents of the ink but will trigger the decomposition of the protective PVP layer and favor the oxidation of SnNPs[42].

After the printing of Sn ink, IPL annealing was conducted by shaping the flashlight spectral output with irradiation energies between 3.3 to 14.1 J/cm². The pulse profile shown in Figure 2a was optimized in order to guarantee ultra-fast heating of Sn and to keep the temperature beneath the maximum working temperature on the backside of the polymer foil. The lifetime of xenon lamps restricts the number of pulses that can be applied successively. Thus, the pulses can be divided into several cycles that are repeated N times at a specific cycling frequency of 4 Hz controlled using the Pulseforge software. Table 1 summarizes the different IPL parameters that were set to deliver a wide range of energies on the printed Sn patterns.

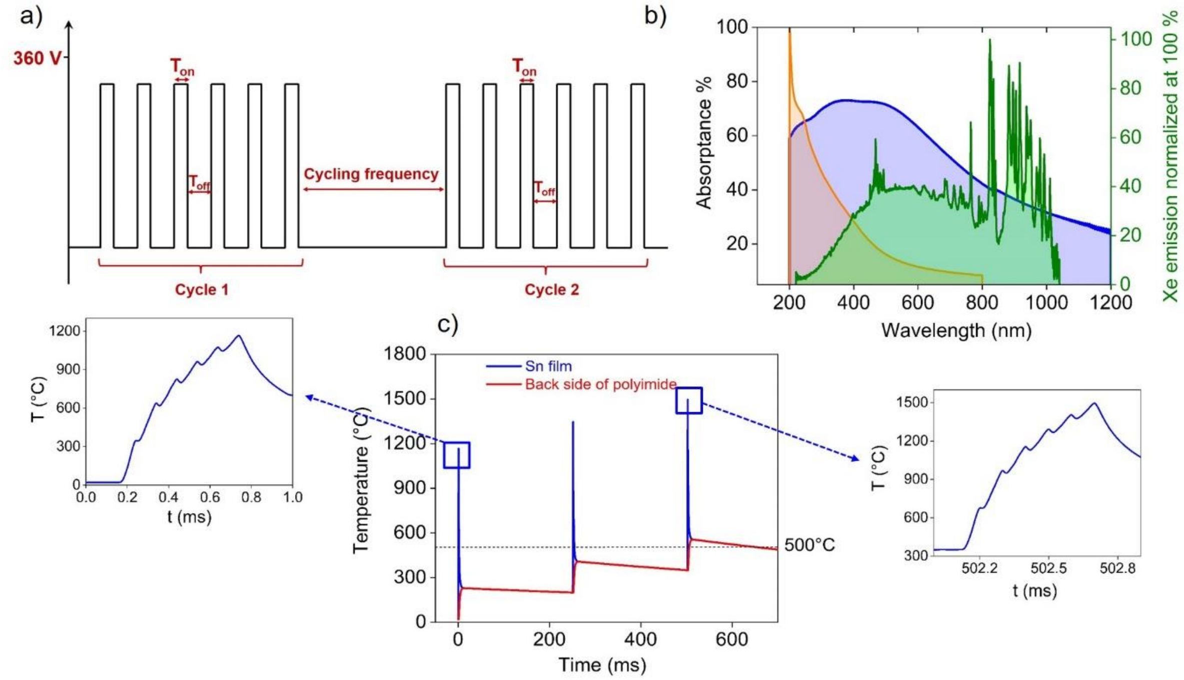

Figure 2. a) Schematic representation of the different parameters of IPL (b) optical absorptance of diluted SnNPs in ethanol (orange) and inkjet-printed SnNPs ink (blue) with the optical emission of xenon flash lamp (green) (c) temperature evolution during IPL: Sn film surface versus back temperature of polyimide for a 3 consecutive IPL cycles (6 pulses in each cycle, cycling frequency = 4 Hz)

Table 1. Different of IPL conditions used to irradiate the printed Sn on Upilex

Conditions	Voltage [V]	Pulse time (T_{on}) [µs]	Pause time (T_{off}) [µs]	Number of pulses/cycle	Number of cycles	Emitted energy [J/cm^2]
1	360	80	20	6	1	3.3
2	360	80	20	10	1	5.2
3	360	80	20	6	2	6.6
4	360	80	20	6	3	9.9
5	360	80	20	8	3	12.84
6	360	80	20	9	3	14.1

The surface temperature during IPL process was numerically computed by solving the transient 1D nonlinear heat transfer equation.

$$\rho_1 Cp_1 \frac{\partial T_1}{\partial t}(x,t) = \frac{\partial}{\partial x}\left(K_1 \frac{\partial T_1}{\partial x}\right) \tag{2}$$

Transient heat flux absorbed by printed SnNPs ink was calculated by equation 3, taking into account the optical absorption of SnNPs, and convection and radiation heat losses thanks to the finite volume method (Supporting Information, section 2).

$$Q(x,t) = \frac{\int \alpha(\lambda) I(\lambda) d\lambda}{\int I(\lambda) d\lambda} \frac{P(t)}{\int P(t) dt} . E(x) \qquad (3)$$

Where α and I are the spectral absorbance of SnNPs and spectral intensity of the xenon lamp, respectively, λ is the wavelength, E is the emitted light energy density measured by a bolometer at the same height as the printed sample and P is the electric power density supplied to the lamp.

Inkjet-printed SnNPs patterns on polymer foil (Upilex®) display broadband light absorption that coincide with the emission spectrum of the xenon lamp (Figure 2b). Indeed, the agglomeration and interparticles coupling of nanoparticles after printing caused the localized surface plasmon resonance peak (λ_{LSPR}= 220 nm) observed for diluted SnNPs to be redshifted and broadened[43], allowing to efficiently absorbing the light emitted by the xenon lamp, which is then converted into heat. From equation (3), an example of power density absorbed by the SnNPs film is plotted in figure S4, according to the emitted power density of the xenon lamps. Figure 2c shows an example of calculated evolution of Sn surface temperature irradiated by a train of 6 pulses repeated 3 times. Thermal properties of Sn and upilex were given in table S1. As expected, a strong photothermal effect by SnNPs produced ultra-fast temperature rise after each pulse through thermal heat flux accumulation. The temperature of the bottom surface of polymer foil was kept cool during the first cycle and then it gradually increased up to 220 °C during the cooling time. The use of a cycling frequency of 4 Hz has been optimized in order to allow the surface to cool down to a certain temperature, before the next cycle restarts, avoiding polymeric substrate degradation. The cooling time was optimized such that the maximum temperature at the rear side of the polymer foil will not exceed the maximum working temperature given around 500 °C.

By increasing emitted light energy density from 3.3 to 14.1 J/cm^2, a tremendous drop of sheet resistance was observed, which was coupled with a linear increase in the temperature of the printed Sn film (Figure 3a). Below the energy density threshold of 6.6 J/cm^2, the sheet resistance decreases rapidly with a large slope. Above 6.6 J/cm^2, the sheet resistance varies slightly but continues to decrease until it reaches a minimum value of 61 ± 2 Ω/sq.

Figure 3a shows that the sheet resistance behavior upon flashing can be attributed to increased surface temperatures. The slope change observed at the energy density of 6.6 J/cm^2 is associated with a calculated temperature of around 1340°C. At this irradiation energy, the color contrast of Sn patterns changed from metal shiny to carbon-like dark grey, as depicted in Figure 3b, which is a synonym for triggering interfacial graphitization of polyimide at the interface with Sn film. Moreover, a progressive widening of the Sn lines printed on the Upilex as a function of the emitted energy is observed in Figures 3b and 3c, which can be attributed to the thermomechanical deformation of the Upilex foil, characterized by a large coefficient of thermal expansion when exposed to high temperature[44,45]. Samples sintered over 14 J/cm^2 (1790°C) exhibit the largest thermomechanical deformation with loss of pattern resolution.

It is worth noting that we tried to generalize this process by testing several type of carbon source. Table S2 shows that Upilex®, printed polyimide ink (PI 6643-001 JNC Corporation), printed carbon ink (Methode Electronics, USA) and fructose can form Sn@G composite under IPL annealing.

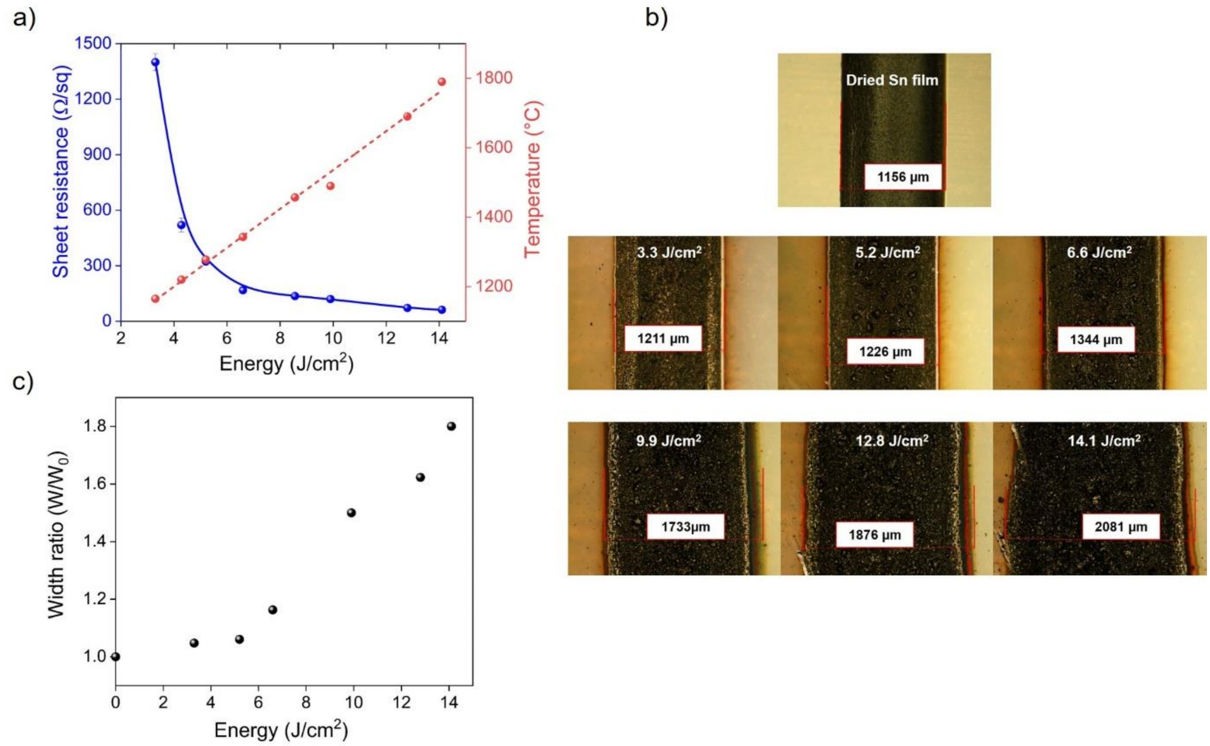

Figure 3 IPL irradiation results of inkjet-printed SnNPs. (a) variation of electrical sheet resistance and simulated temperature as a function of the irradiated energy. (b) optical micrographs of the printed Sn lines upon increasing irradiation energy (c) corresponding lines width variation (W_0 is the width of the dried Sn film – W is the width of the irradiated Sn film).

Raman spectroscopy was then performed to trace the carbon supply into Sn patterns upon IPL annealing (Figure 4a). For energies below 6.6 J/cm², the distinctive G (1598 cm^{-1}, graphitic carbon), D (1350 cm^{-1}, defective carbon) bands and the very low and broad 2D peak are the signature of nanocrystalline graphitic carbon domains in an amorphous tetrahedral carbon matrix[46–48]. This is a clear indication of the role of polyimide as precursor feeding carbon atoms into SnNPs. Increasing radiant energy above 6.6 J/cm² induces a gradual collapse of defect-related D peak and the enhancement of G peak. The decline of the I_D/I_G ratio from 1.02 to an optimal value of 0.22 indicates substantial defects healing and carbon crystallization (Figure 4b). The emergence of a sharp 2D peak fitting into a single Lorentzian shape could be attributed to the formation of monolayer graphene or to multi-layer graphene/ disordered graphite along the c-axis[49,50]. The position of the 2D peak at 2705 cm^{-1} and the FWHM of 43 cm^{-1} (at 12 J/cm²) are different from values reported for monolayer graphene (2D peak position at 2680 cm^{-1}, FWHM(2D) = 30 cm^{-1})[50,51]. This indicates that IPL sintering of SnNPs on polyimide produced multi-layer graphene/ disordered graphite randomly stacked with weak interaction. The absence of interlayer coupling can be beneficial as few-layer graphene exhibits electronic properties similar to that of monolayer graphene[52].

Cross-sectional TEM image of the Sn@G film irradiated by 12.8 J/cm^2 depicted in Figure 4c shows that spheroid-like SnNPs have agglomerated near the surface with sizes close to the initial distribution. We observe that these NPs are embedded in the polymer matrix during IPL treatment, which can be justified by the viscoelastic deformation of Upilex foil characterized by a high out-of-plane thermal expansion coefficient compared to the in-plane one and a glass transition around 300°C[45]. Figure 4b reveals the presence of 3-4 planes surrounding the SnNPs with a spacing of ~0.34 nm, close to the interlayer spacing values of the graphene planes. We also notice the dissolution of native tin oxide shell layer standing on SnNPs, most probably thanks to the carbothermal reduction process. The following chemical reaction could occur at the surface of the molten Sn:

$$SnO_{2(s)} + C_{(s)} \rightarrow Sn_{(l)} + 2CO_{(g)}$$

We believe that this assumption is paired with the enhancement of the electrical conductivity of light flashed Sn films. The native tin oxide is replaced with the graphene shell acting as an excellent conductor, which will enhance electron transport in printed Sn film.

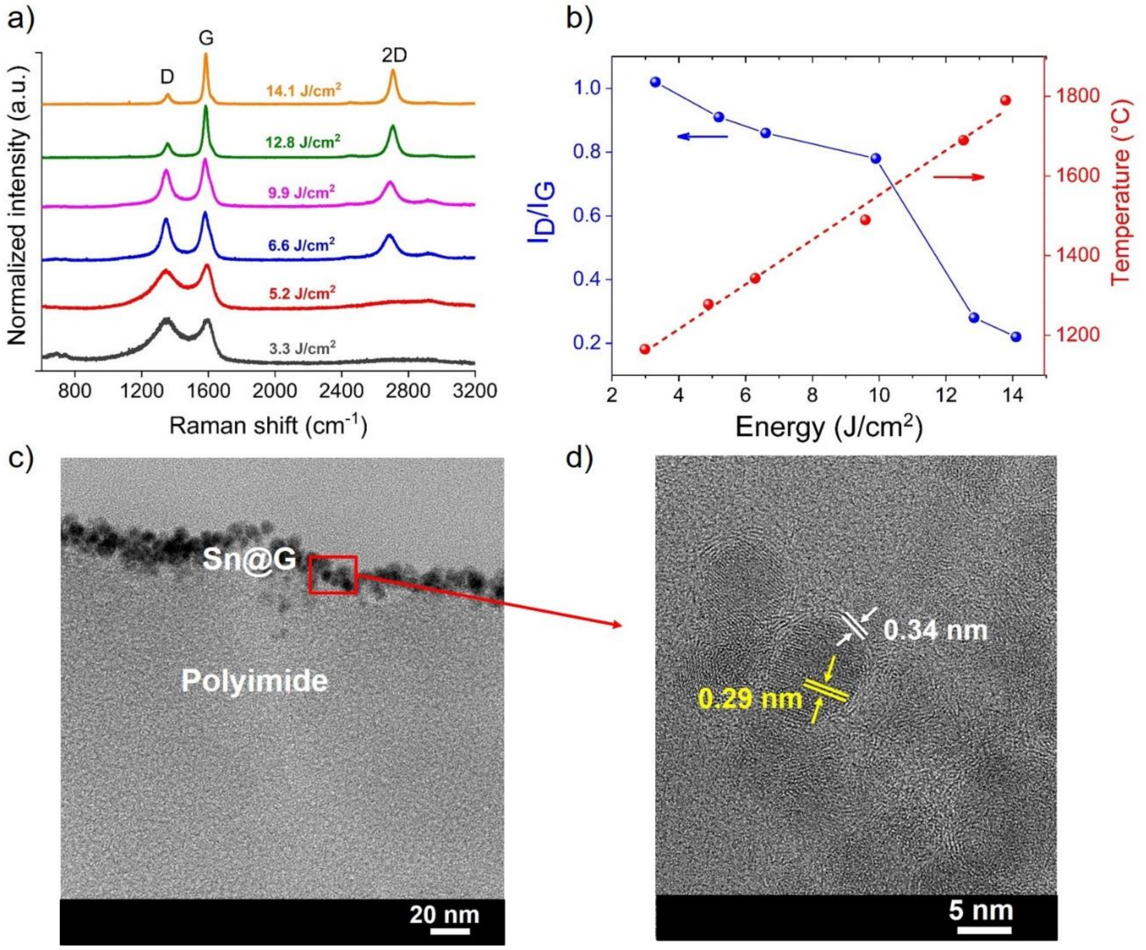

Figure 4 (a) evolution of Raman spectra with flashlight condition at fixed voltage 360 V (b) evolution of I_D/I_G ratio and temperature with applied energy density (c) TEM cross section and (d) HRTEM of Sn@G film formed after IPL annealing at 12.8 J/cm^2

Owing to these findings, Sn@G material was evaluated as electrodes for next generation energy harvesting and storage devices such as flexible LIB. These Sn@G electrodes were fabricated on polyimide by irradiating SnNPs ink with energy of 12.8 J/cm². Figure 5a shows typical galvanostatic charge/discharge profile of the Sn@G electrodes at a current rate of C/10 (1C=1A/g). The first discharge and charge cycles deliver high specific capacity of 2205 mAh/g and 1012 mAh/g, respectively. The initial irreversible capacity loss (50%) can be mainly attributed to the formation of a solid–electrolyte interface (SEI) at the electrode surface, which is induced by the decomposition of the liquid organic electrolyte at low potentials. These side reactions are well known to consume Li ions and are responsible for the continuous growth of an insulating barrier at the surface of the anode that hinders the electron transfer and leads to decreased specific capacity[53]. After the first cycle, the charge/discharge curves nearly overlap thus suggesting excellent cycling stability. The capacity retention from the second to the 10th cycles increases from 93% to 97%.

Moreover, the SnNP@G electrode exhibits excellent cycling performances as depicted in Figure 5b. As the current density increases from 100 to 200 and 500 mA/g, the Sn@G electrode shows high discharge capacity with values varying from 1073 mAh/g to 815 mAh/g and 750 mAh/g, respectively. Finally, the capacity tends to recover back to a value of 900 mAh/g in the 50th cycle when the current density step back to 100 mA/g, thus recovering almost 88% of its initial specific capacity. The long-term cycling performance of Sn@G at high charge/discharge rates of 1 A/g have been investigated (Figure 5c). After initial capacity decay during the first 10th cycle, the Sn@G electrode exhibits a reversible capacity of 1017 mAh/g for 100 cycles. This specific capacity is 67% higher than that of the commonly used lithiated graphites (LiC6). The Coulombic efficiency reaching almost 100% at such high rate, demonstrating excellent Li-storage capability and cycling performance of our Sn@G hybrid electrode.

In parallel, electrochemical impedance spectroscopy has also been performed for Sn@G electrodes after 1 and 100 cycles (Supporting Information, Figure S5a). The Nyquist plots consist of semi-circles in the medium-high frequency region, which is the signature of the charge transfer impedance and the SEI layer. The low-frequency straight line represents the signature of Li diffusion, which can be modelled by Warburg-type diffusion impedance. A modified Randles circuit has been used to model the impedance spectra (Supporting Information, Figure S5b and Table S3). The values of the charge transfer resistance R_{CT} vary from 480Ω to 352 Ω after 1 cycle and 100 cycles, respectively. The decrease of R_{CT} after 100 cycles implies that the material is activated during the lithiation/de-lithiation process and that the process of lithium storage is improved. In addition, the measured lithium ion diffusion coefficient is significantly enhanced upon cycling (670 Ω $\mathrm{rad}^{1/2}\mathrm{s}^{-1/2}$ after 1 cycle, 360 Ω $\mathrm{rad}^{1/2}\mathrm{s}^{-1/2}$ after 100 cycles), indicating efficient lithium ion kinetics in the Sn@G electrode.

Finally, STEM and HRTEM images of the cycled Sn@G electrode at 1C show that the electrode is still covering the surface of the polyimide (Supporting Information, Figure S6), without any noticeable volume expansion or aggregation. The nanoparticles covered with the graphene film present the same diameter as the one measured before lithiation. This result confirms the role of the graphene as an excellent mechanical capping layer that protect Sn nanoparticles against aggregation and pulverization.

The electrochemical properties of Sn@G electrodes are compared to that of previous reports on other hybrid Sn/graphene anodes (Supporting Information, Table S4). We believe these excellent electrochemical performances are the result of the synergetic effect between high quality few-layered graphene conformally confining the monodisperse SnNPs. In fact, most of the Sn/graphene hybrid anodes rely on the use of reduced graphene oxide (RGO) sheets to support or wrap the SnNPs (Sn@RGO) at a certain degree. The use of a high quality nitrogen doping graphene layer (NG)[54], Sn sheets confined by graphene in 2D/2D configuration[55], has proven to improve the long-term cycling stability. The best results achieved in 0D/2D Sn based hybrid nanostructures show a specific capacity of 568 mAh/g after 1000 cycles at 1A/g[56]. To the best of our knowledge, phosphating SnNPs and their encapsulation with high quality N-doped graphene sheet to form P-Sn/NG show superior electrochemical properties with a specific capacity of 1083.9 mAh/g after 500 cycle at 1A/g[57], which is very close to our results on Sn@G electrodes.

In fact, our process offers the capability of producing Sn@G electrodes additively on any substrate including plastic sheets without the use of GO material, which is a clear asset toward the fabrication of LIB on flexible substrate. Moreover, there is no need to use chemical binders for the material and the printed Sn@G anode can be used directly as current collector, thus removing the problems related to cracks and pulverization observed at the interface between current collector (like aluminum or copper foil) and the Sn-based hybrid material.

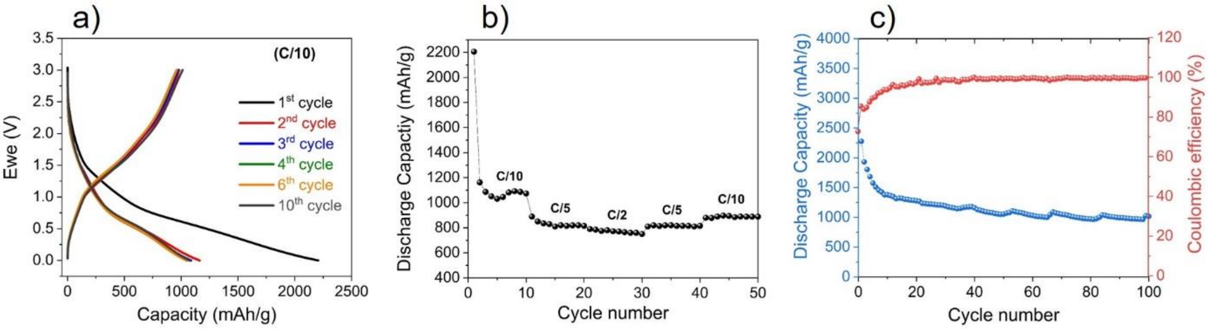

Figure 5 performances of Sn@G material as anode for Lithium ion battery (a) charge/discharge profile of Sn@G electrode at C/10 (b) electrochemical performance of at multi C-rates (c) discharge capacity values and coulombic efficiency variations for 100 cycles at 1C

Apart from LIB applications, Sn@G could be an appropriate candidate for energy harvesting devices such as triboelectric nanogenerators (TENG). With the printed SnNPs patterns providing huge advantages without any complex patterning or lithographic techniques, it can efficiently generate triboelectric charges on its surface. Additionally, the Sn@G composite also acts as the electrode of the TENG, removing the need for an electrode preparation process. A single operational cycle can be explained by coupling contact electrification and electrostatic induction effects, inducing a flow of charges through an external load[58]. The electrical performances of TENG based Sn@G are shown in figure 6a-b. A stable open-circuit voltage of 150 V and short-circuit current of 5.8 μA was generated on a 4 cm² contact surface area, comparable to results obtained for TENGs with conventional gold electrode evaporated on polyimide foil. Figure 6c illustrates the comparison of the output power of Sn@G and Au electrode as a function of load impedance. With a peak power of 50 μW at 10 MΩ, the generated power density of about 125 mW/m² could either be stored or directly used to drive small-scale electronics. In addition, a durability test over 10000 cycles confirm the very good electrical and mechanical stability (Supporting Information, Figure S7). It should be mentioned that the obtained power density is within the same order of magnitude as the values reported for different TENG structures that use graphene alone and graphene nano-composite as electrodes on different polymer substrates (Supporting Information, Table S5).

The working mechanism of the Sn@G-TENG is illustrated in figure 6c. When films were brought into contact by mechanical compression, triboelectric charges with opposite signs are generated. As a tribo-negative material, upilex will pump electrons from Sn@G, which results in a build-up of a negatively charged upilex surface and positively charged Sn@G electrode. These opposite charges compensate each other and no electrical signal is generated. Next, the release of the mechanical force will generate a strong electric potential difference that is compensated by driving the electrons to flow from the bottom Sn@G electrode (positive potential) into the top one (negative potential), through an external circuit. The next mechanical compression drives the electrons to flow in the opposite direction (from to negatively to positively charged electrode) since the electric potential difference is reduced. Thus, the mechanical cycling of TENG will provide an AC current that flow from both Sn@G electrodes via an external load.

By comparison, the TENG made by gold-upilex system show electrical performances similar to that of Sn@G material. This can be explained by their work functions which has similar values ($\varphi_{Sn@G}$= 4.7 eV and φ_{Au}= 4.6 eV). Meanwhile, Sn@G electrode represents the advantage of being able to be manufactured using additive technology where other set of nanoparticles@graphene system can be engineered in the future.

This study demonstrated one-of-its kind progress in the enhancement of the output power of TENGs by using a simple printing technique with organic/inorganic hybrid materials, which may open new avenues of research for triboelectric materials. Our future work will focus on developing multi-layer TENGs based on Sn@G for large-scale active sensors and portable electronics.

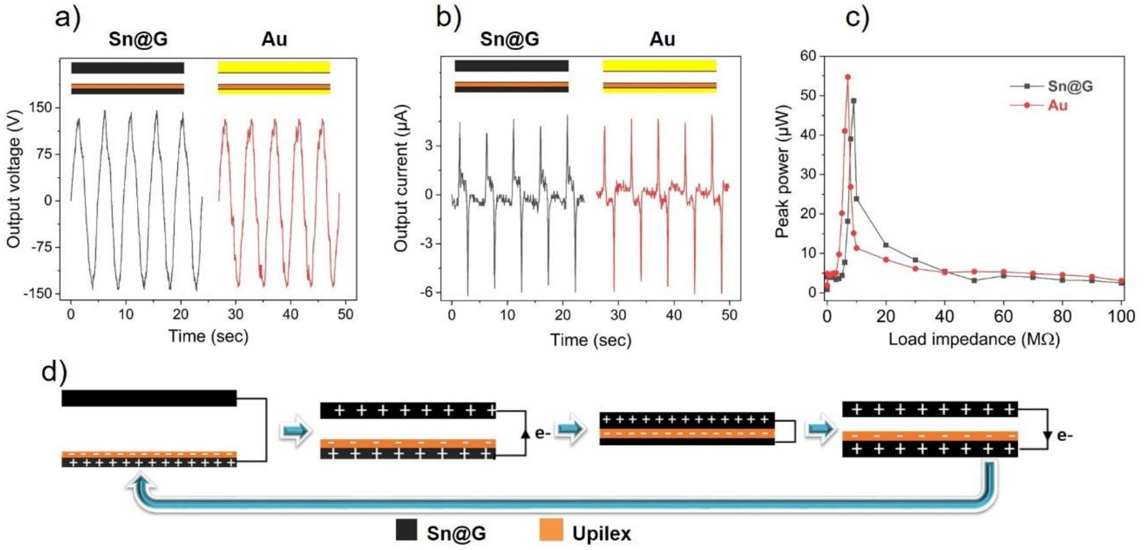

Figure 6. performances of Sn@G material as electrode for triboelectric nanogenerator (a-b) comparison of output voltage and current of TENGs with Sn@G and gold electrodes (c) comparison of output power from Sn@G and gold electrodes and their dependence on the external loads (d) working mechanism of contact–separation TENG.

Conclusion

In summary, we have successfully demonstrated a new method to fabricate hybrid Sn@G on plastic directly from inkjet-printed Sn patterns at ambient condition. The intensive light absorbed by SnNPs yield extreme localized heat on the upper surface of the polyimide, which carbonize and act as a local carbon precursor feeding beneath SnNPs patterns. Thermally activated carbon atoms diffuse and wrap into SnNPs thus forming Sn@G core-shell hybrid material on plastic. We demonstrate the powerf of the method for the fabrication of flexible electrodes for lithium ion batteries and triboelectric nanogenerators. Beyond Sn and polyimide, this scalable and straightforward method offers versatile approach that can be extended to other graphene-nanoparticles hybrids by choosing different nanoparticles and solid carbon sources.

Supporting Information

TGA/DSC curves, surface energy and inkjet printing of Sn ink, numerical modelling of temperature and thermal properties of materials, electrochemical impedance, TEM images, TENG stability, literature survey of lithium ion battery and triboelectric nanogenerator devices.

References

(1) Novoselov, K. S.; Geim, A. K.; Morozov, S. V.; Jiang, D.; Zhang, Y.; Dubonos, S. V.; Grigorieva, I. V.; Firsov, A. A. Electric Field Effect in Atomically Thin Carbon Films. *Sci. New Ser.* **2004**, *306* (5696,), 666–669.

(2) Novoselov, K. S.; Fal′ko, V. I.; Colombo, L.; Gellert, P. R.; Schwab, M. G.; Kim, K. A Roadmap for Graphene. *Nature* **2012**, *490* (7419), 192–200.

(3) Randviir, E. P.; Brownson, D. A. C.; Banks, C. E. A Decade of Graphene Research: Production, Applications and Outlook. *Mater. Today* **2014**, *17* (9), 426–432.

(4) Giovannetti, G.; Khomyakov, P. A.; Brocks, G.; Karpan, V. M.; van den Brink, J.; Kelly, P. J. Doping Graphene with Metal Contacts. *Phys. Rev. Lett.* **2008**, *101* (2), 026803.

(5) Liu, Z.; Liu, Q.; Huang, Y.; Ma, Y.; Yin, S.; Zhang, X.; Sun, W.; Chen, Y. Organic Photovoltaic Devices Based on a Novel Acceptor Material: Graphene. *Adv. Mater.* **2008**, *20* (20), 3924–3930.

(6) Li, X.; Zhang, G.; Bai, X.; Sun, X.; Wang, X.; Wang, E.; Dai, H. Highly Conducting Graphene Sheets and Langmuir–Blodgett Films. *Nat. Nanotechnol.* **2008**, *3* (9), 538–542.

(7) Lu, Z.; Guo, C. X.; Yang, H. B.; Qiao, Y.; Guo, J.; Li, C. M. One-Step Aqueous Synthesis of Graphene–CdTe Quantum Dot-Composed Nanosheet and Its Enhanced Photoresponses. *J. Colloid Interface Sci.* **2011**, *353* (2), 588–592.

(8) Bajpai, R.; Roy, S.; Kumar, P.; Bajpai, P.; Kulshrestha, N.; Rafiee, J.; Koratkar, N.; Misra, D. S. Graphene Supported Platinum Nanoparticle Counter-Electrode for Enhanced Performance of Dye-Sensitized Solar Cells. *ACS Appl. Mater. Interfaces* **2011**, *3* (10), 3884–3889.

(9) Li, Y.-A.; Chen, Y.-J.; Tai, N.-H. Fast Process To Decorate Silver Nanoparticles on Carbon Nanomaterials for Preparing High-Performance Flexible Transparent Conductive Films. *Langmuir* **2013**, *29* (26), 8433–8439.

(10) Wang, H.; Cui, L.-F.; Yang, Y.; Sanchez Casalongue, H.; Robinson, J. T.; Liang, Y.; Cui, Y.; Dai, H. Mn_3O_4 −Graphene Hybrid as a High-Capacity Anode Material for Lithium Ion Batteries. *J. Am. Chem. Soc.* **2010**, *132* (40), 13978–13980.

(11) Raccichini, R.; Varzi, A.; Passerini, S.; Scrosati, B. The Role of Graphene for Electrochemical Energy Storage. *Nat. Mater.* **2015**, *14* (3), 271–279.

(12) Liang, Y. Co3O4 Nanocrystals on Graphene as a Synergistic Catalyst for Oxygen Reduction Reaction. *Nat. Mater.* **2011**, *10*, 7.

(13) Yu, Y.; Chen, Z.; He, S.; Zhang, B.; Li, X.; Yao, M. Direct Electron Transfer of Glucose Oxidase and Biosensing for Glucose Based on PDDA-Capped Gold Nanoparticle Modified Graphene/Multi-Walled Carbon Nanotubes Electrode. *Biosens. Bioelectron.* **2014**, *52*, 147–152.

(14) Jang, H.; Park, Y. J.; Chen, X.; Das, T.; Kim, M.-S.; Ahn, J.-H. Graphene-Based Flexible and Stretchable Electronics. *Adv. Mater.* **2016**, *28* (22), 4184–4202.

(15) McManus, D.; Vranic, S.; Withers, F.; Sanchez-Romaguera, V.; Macucci, M.; Yang, H.; Sorrentino, R.; Parvez, K.; Son, S.-K.; Iannaccone, G.; Kostarelos, K.; Fiori, G.;

Casiraghi, C. Water-Based and Biocompatible 2D Crystal Inks for All-Inkjet-Printed Heterostructures. *Nat. Nanotechnol.* **2017**, *12* (4), 343–350.

(16) Arias, A. C.; MacKenzie, J. D.; McCulloch, I.; Rivnay, J.; Salleo, A. Materials and Applications for Large Area Electronics: Solution-Based Approaches. *Chem. Rev.* **2010**, *110* (1), 3–24.

(17) Khan, Y.; Thielens, A.; Muin, S.; Ting, J.; Baumbauer, C.; Arias, A. C. A New Frontier of Printed Electronics: Flexible Hybrid Electronics. *Adv. Mater.* **2020**, *32* (15), 1905279.

(18) Moses, O. A.; Gao, L.; Zhao, H.; Wang, Z.; Lawan Adam, M.; Sun, Z.; Liu, K.; Wang, J.; Lu, Y.; Yin, Z.; Yu, X. 2D Materials Inks toward Smart Flexible Electronics. *Mater. Today* **2021**, *50*, 116–148.

(19) Liu, Q.; Wei, L.; Wang, J.; Peng, F.; Luo, D.; Cui, R.; Niu, Y.; Qin, X.; Liu, Y.; Sun, H.; Yang, J.; Li, Y. Cell Imaging by Graphene Oxide Based on Surface Enhanced Raman Scattering. *Nanoscale* **2012**, *4* (22), 7084.

(20) Shen, J.; Yan, B.; Shi, M.; Ma, H.; Li, N.; Ye, M. One Step Hydrothermal Synthesis of TiO2-Reduced Graphene Oxide Sheets. **2011**, 21, 3415-3421.

(21) Niu, Z.; Du, J.; Cao, X.; Sun, Y.; Zhou, W.; Hng, H. H.; Ma, J.; Chen, X.; Xie, S. Electrophoretic Build-Up of Alternately Multilayered Films and Micropatterns Based on Graphene Sheets and Nanoparticles and Their Applications in Flexible Supercapacitors. *Small* **2012**, *8* (20), 3201–3208.

(22) Chen, W.; Li, S.; Chen, C.; Yan, L. Self-Assembly and Embedding of Nanoparticles by In Situ Reduced Graphene for Preparation of a 3D Graphene/Nanoparticle Aerogel. *Adv. Mater.* **2011**, *23* (47), 5679–5683.

(23) Son, J. Y.; Shin, Y.-H.; Kim, H.; Jang, H. M. NiO Resistive Random Access Memory Nanocapacitor Array on Graphene. *ACS Nano* **2010**, *4* (5), 2655–2658.

(24) Allain, A.; Han, Z.; Bouchiat, V. Electrical Control of the Superconducting-to-Insulating Transition in Graphene–Metal Hybrids. *Nat. Mater.* **2012**, *11* (7), 590–594.

(25) Li, M.; Li, X.; Li, W.; Meng, X.; Yu, Y.; Sun, X. Atomic Layer Deposition Derived Amorphous TiO2 Thin Film Decorating Graphene Nanosheets with Superior Rate Capability. *Electrochem. Commun.* **2015**, *57*, 43–47.

(26) Schniepp, H. C.; Li, J.-L.; McAllister, M. J.; Sai, H.; Herrera-Alonso, M.; Adamson, D. H.; Prud'homme, R. K.; Car, R.; Saville, D. A.; Aksay, I. A. Functionalized Single Graphene Sheets Derived from Splitting Graphite Oxide. *J. Phys. Chem. B* **2006**, *110* (17), 8535–8539.

(27) Konios, D.; Stylianakis, M. M.; Stratakis, E.; Kymakis, E. Dispersion Behaviour of Graphene Oxide and Reduced Graphene Oxide. *J. Colloid Interface Sci.* **2014**, *430*, 108–112.

(28) Stankovich, S.; Dikin, D. A.; Piner, R. D.; Kohlhaas, K. A.; Kleinhammes, A.; Jia, Y.; Wu, Y.; Nguyen, S. T.; Ruoff, R. S. Synthesis of Graphene-Based Nanosheets via Chemical Reduction of Exfoliated Graphite Oxide. *Carbon* **2007**, *45* (7), 1558–1565.

(29) Mkhoyan, K. A.; Contryman, A. W.; Silcox, J.; Stewart, D. A.; Eda, G.; Mattevi, C.; Miller, S.; Chhowalla, M. Atomic and Electronic Structure of Graphene-Oxide. *Nano Lett.* **2009**, *9* (3), 1058–1063.

(30) Cortie, M. B.; Coutts, M. J.; Ton-That, C.; Dowd, A.; Keast, V. J.; McDonagh, A. M. On the Coalescence of Nanoparticulate Gold Sinter Ink. *J. Phys. Chem. C* **2013**, *117* (21), 11377–11384.

(31) Tao, Y.; Tao, Y.; Wang, B.; Wang, L.; Tai, Y. A Facile Approach to a Silver Conductive Ink with High Performance for Macroelectronics. *Nanoscale Res. Lett.* **2013**, 8:296.

(32) Shirai, H.; Nguyen, M. T.; Ishida, Y.; Yonezawa, T. A New Approach for Additive-Free Room Temperature Sintering of Conductive Patterns Using Polymer-Stabilized Sn Nanoparticles. *J. Mater. Chem. C* **2016**, *4* (11), 2228–2234.

(33) Vishwakarma, R.; Rosmi, M. S.; Takahashi, K.; Wakamatsu, Y.; Yaakob, Y.; Araby, M. I.; Kalita, G.; Kitazawa, M.; Tanemura, M. Transfer Free Graphene Growth on SiO2 Substrate at 250 °C. *Sci. Rep.* **2017**, *7* (1). https://doi.org/10.1038/srep43756.

(34) Po-Chun Huang; Jenq-Gong Duh. Effects of Different Surfactant Additions and Treatments on the Characteristics of Tin Nanosolder by Chemical Reduction Method. In *2008 58th Electronic Components and Technology Conference*; IEEE: Lake Buena Vista, FL, USA, 2008; pp 431–435.

(35) Chee, S.-S.; Lee, J.-H. Synthesis of Sub-10-Nm Sn Nanoparticles from Sn(II) 2-Ethylhexanoate by a Modified Polyol Process and Preparation of AgSn Film by Melting of the Sn Nanoparticles. *Thin Solid Films* **2014**, *562*, 211–217.

(36) Sánchez, S. A.; Narciso, J.; Louis, E.; Rodríguez-Reinoso, F.; Saiz, E.; Tomsia, A. Wetting and Capillarity in the Sn/Graphite System. *Mater. Sci. Eng. A* **2008**, *495* (1–2), 187–191.

(37) Xu, Y.; Liu, Q.; Zhu, Y.; Liu, Y.; Langrock, A.; Zachariah, M. R.; Wang, C. Uniform Nano-Sn/C Composite Anodes for Lithium Ion Batteries. *Nano Lett.* **2013**, *13* (2), 470–474.

(38) Derby, B. Inkjet Printing of Functional and Structural Materials: Fluid Property Requirements, Feature Stability, and Resolution. *Annu. Rev. Mater. Res.* **2010**, *40* (1), 395–414..

(39) Pastoriza-Santos, I.; Liz-Marzán, L. M. Formation of PVP-Protected Metal Nanoparticles in DMF. *Langmuir* **2002**, *18* (7), 2888–2894.

(40) Matavž, A.; Frunză, R. C.; Drnovšek, A.; Bobnar, V.; Malič, B. Inkjet Printing of Uniform Dielectric Oxide Structures from Sol–Gel Inks by Adjusting the Solvent Composition. *J. Mater. Chem. C* **2016**, *4* (24), 5634–5641.

(41) Kassem, O.; Saadaoui, M.; Rieu, M.; Sao-Joao, S.; Viricelle, J. P. Synthesis and Inkjet Printing of Sol–Gel Derived Tin Oxide Ink for Flexible Gas Sensing Application. *J. Mater. Sci.* **2018**, *53* (18), 12750–12761.

(42) Jo, Y. H.; Jung, I.; Choi, C. S.; Kim, I.; Lee, H. M. Synthesis and Characterization of Low Temperature Sn Nanoparticles for the Fabrication of Highly Conductive Ink. *Nanotechnology* **2011**, *22* (22), 225701.

(43) Pazos-Perez, N.; Wagner, C. S.; Romo-Herrera, J. M.; Liz-Marzán, L. M.; García de Abajo, F. J.; Wittemann, A.; Fery, A.; Alvarez-Puebla, R. A. Organized Plasmonic Clusters with High Coordination Number and Extraordinary Enhancement in Surface-Enhanced Raman Scattering (SERS). *Angew. Chem.* **2012**, *124* (51), 12860–12865.

(44) Chen, S. T.; Wagner, H. H. Out-of-Plane Thermal Expansion Coefficient of Biphenyldianhydride-Phenylenediamine Polyimide Film. *J. Electron. Mater.* **1993**, *22* (7), 797–799..

(45) Kassem, O.; Saadaoui, M.; Rieu, M.; Viricelle, J.-P. A Novel Approach to a Fully Inkjet Printed SnO_2 -Based Gas Sensor on a Flexible Foil. *J. Mater. Chem. C* **2019**, *7* (39), 12343–12353.

(46) Lespade, P.; Al-Jishi, R.; Dresselhaus, M. S. Model for Raman Scattering from Incompletely Graphitized Carbons. *Carbon* **1982**, *20* (5), 427–431.

(47) Ferrari, A. C.; Robertson, J. Interpretation of Raman Spectra of Disordered and Amorphous Carbon. *Phys. Rev. B* **2000**, *61* (20), 14095–14107.

(48) Sadezky, A.; Muckenhuber, H.; Grothe, H.; Niessner, R.; Pöschl, U. Raman Microspectroscopy of Soot and Related Carbonaceous Materials: Spectral Analysis and Structural Information. *Carbon* **2005**, *43* (8), 1731–1742.

(49) Cançado, L. G.; Takai, K.; Enoki, T.; Endo, M.; Kim, Y. A.; Mizusaki, H.; Speziali, N. L.; Jorio, A.; Pimenta, M. A. Measuring the Degree of Stacking Order in Graphite by Raman Spectroscopy. *Carbon* **2008**, *46* (2), 272–275.

(50) Ferrari, A. C.; Meyer, J. C.; Scardaci, V.; Casiraghi, C.; Lazzeri, M.; Mauri, F.; Piscanec, S.; Jiang, D.; Novoselov, K. S.; Roth, S.; Geim, A. K. Raman Spectrum of Graphene and Graphene Layers. *Phys. Rev. Lett.* **2006**, 97, 187401.

(51) Malard, L. M.; Pimenta, M. A.; Dresselhaus, G.; Dresselhaus, M. S. Raman Spectroscopy in Graphene. *Phys. Rep.* **2009**, *473* (5–6), 51–87.

(52) Hass, J.; Varchon, F.; Millán-Otoya, J. E.; Sprinkle, M.; Sharma, N.; de Heer, W. A.; Berger, C.; First, P. N.; Magaud, L.; Conrad, E. H. Why Multilayer Graphene on 4 H − SiC (000 $\bar{1}$) Behaves Like a Single Sheet of Graphene. *Phys. Rev. Lett.* **2008**, *100* (12), 125504.

(53) Winter, M.; Besenhard, J. O. Electrochemical Lithiation of Tin and Tin-Based Intermetallics and Composites. *Electrochimica Acta* **1999**, *45* (1–2), 31–50..

(54) Zhou, X.; Bao, J.; Dai, Z.; Guo, Y.-G. Tin Nanoparticles Impregnated in Nitrogen-Doped Graphene for Lithium-Ion Battery Anodes. *J. Phys. Chem. C* **2013**, *117* (48), 25367–25373.

(55) Bin, L.; Bin, W.; Xianglong, L.; Yuying, J.; Minghui, L.; Linjie, Z. Graphene-Confined Sn Nanosheets with Enhanced Lithium Storage Capability. *Adv. Mater.* **2012**, *24* (41), 5525–5525.

(56) Liu, L.; Huang, X.; Guo, X.; Mao, S.; Chen, J. Decorating in Situ Ultrasmall Tin Particles on Crumpled N-Doped Graphene for Lithium-Ion Batteries with a Long Life Cycle. *J. Power Sources* **2016**, *328*, 482–491.

(57) Kong Z.; Zhang K.; Huang M.; Tu H.; Yao X.; Shao Y.; Wu Y.; Hao X. Stabilizing Sn anodes nanostructure: Structure optimization and interfacial engineering to boost lithium storage. *Electrochemica Acta.* **2022**, 405 139789

(58) Ravichandran, A. N.; Ramuz, M.; Blayac, S. Increasing Surface Charge Density by Effective Charge Accumulation Layer Inclusion for High-Performance Triboelectric Nanogenerators. *MRS Commun.* **2019**, *9* (2), 682–689.